silicides, germanides and water frameworks suggest that the area per vertex, Ω, varies little as a function of the framework curvature, for a fixed framework composition (Hyde, 1993).

From O'Keeffe's (1991) network classification, the average surface ring size for the minimal embedding of any network containing equivalent vertices (or, alternatively, the characteristic of the network, γ) can be readily determined (Hyde, 1993). The area per vertex, Ω, can then be deduced from (4) and (7). Where more than one type of vertex is present in a net, upper and lower bounds on the average surface ring size can be found. Fig. 3 shows the area, Ω, of a range of silicon-rich zeolites, clathrasils and dense silicates, using standard data for the framework density, assuming a distance of 3.05 Å between the T-atom vertices. With the exception of the densest four-connected silicate framework, coesite, the frameworks exhibit approximately equal area per vertex, regardless of the curvature of the framework.

These data are plotted with the maximum and minimum areas found according to (9) and (14) in Fig. 4. Geometrical considerations alone allow the areas to vary between these limits, under the assumption of quasi-uniform networks. Clearly, the weak variation of surface areas with silica-framework curvature is not due to the geometry of Euclidean three-dimensional space. Rather, this effect must be set by interatomic interactions at work within these covalent frameworks.

I thank Professor Michael O'Keeffe for many stimulating discusssions.

References

ANDERSSON, S., HYDE, S. T., LARSSON, K. & LIDIN, S. (1988). *Chem. Rev.* **88**, 221–242.

BRUNNER, G. O. & MEIER, W. M. (1989). *Nature (London)*, **337**, 146–147.

COXETER, H. S. M. (1937). *Proc. London Math. Soc. Second Ser.* **43**, 33–62.

FIRBY, P. A. & GARDINER, C. F. (1991). *Surface Topology*. Chichester: Ellis Horwood Ltd.

HYDE, S. T. (1992). *Pure Appl. Chem.* **64**(11), 1617–1622.

HYDE, S. T. (1993). *Defects and Processes in the Solid State. Some Examples in Earth Sciences*, edited by J. BOLAND & J. FITZGERALD, pp. 317–342. Amsterdam: Elsevier.

HYDE, S. T. & ANDERSSON, S. (1984). *Z. Kristallogr.* **168**, 221–254.

HYDE, S. T., BLUM, Z. & NINHAM, B. W. (1993). *Acta Cryst.* A**49**, 586–589.

LENOSKY, T., GONZE, X., TETER, M. & ELSER, V. (1992). *Nature (London)*, **355**, 333–335.

LINDSAY, J. H. (1959). *Am. Math. Mon.* **36**, 117–118.

MACKAY, A. L. & TERRONES, H. (1993). *Philos. Trans. R. Soc. London (Phys. Eng.)*, **343**, 113–127.

MEIER, W. M. (1986). *Pure Appl. Chem.* **58**, 1323–1328.

MEIER, W. M. & OLSON, D. H. (1992). *Atlas of Zeolite Structure Types*. London: Butterworth–Heinemann.

O'KEEFFE, M. (1991). *Z. Kristallogr.* **196**, 21–37.

O'KEEFFE, M., ADAMS, G. B. & SANKEY, O F. (1992). *Phys. Rev. Lett.* **68**(15), 2325–2328.

O'KEEFFE, M. & HYDE, B. G. (1994). Book to be published by World Scientific Press, Singapore.

ROBERTSON, H. P. (1990). *The Encyclopedia of Physics*, p. 266. New York: Simon and Schuster.

SMITH, J. V. (1988). *Chem. Rev.* **88**, 149–182.

STIXRUDE, L. & BUKOWINSKI, M. S. T. (1990). *Am. Mineral.* **75**, 1159–1169.

TERRONES, H. & MACKAY, A. L. (1993). *Chem. Phys. Lett.* **207**(1), 45–50.

VANDERBILT, D. & TERSOFF, J. (1991). *Phys. Rev. Lett.* **68**, 511–513.

WELLS, A. F. (1977). *Three-Dimensional Nets and Polyhedra*, p. 160. New York: Wiley.

Acta Cryst. (1994). A**50**, 759–771

On the Validity of the Direct Phasing and Fourier Method in Electron Crystallography

BY L.-M. PENG AND S. Q. WANG*

Department of Materials, University of Oxford, Parks Road, Oxford OX1 3PH, England

(*Received* 31 *January* 1994; *accepted* 25 *May* 1994)

Abstract

The validity of the direct phasing and Fourier method for direct crystal structure determination is examined. It is shown that, while the kinematic approximation for electron diffraction is not strictly valid for all materials containing heavy atoms in real space, many of the low-order diffracted beams behave kinematically for a small crystal thickness. For thin crystals, structure maps constructed from compound crystals containing heavy atoms using low-order reflections are found to be faithful representations of the crystal structures. The inclusion of high-order diffracted beams is shown, however, to introduce intensity maxima that do not coincide with atom positions. It is shown that, if dynamical phases

* Also at Beijing Laboratory of Electron Microscopy, Chinese Academy of Sciences, Beijing, People's Republic of China.

ISSN 0108-7673 ©1994

of the diffracted beams are available, as in the case of electron holography, an electron-density map using dynamical phases is a better map of the crystal structure than the structure map constructed using kinematic phases.

1. Introduction

It has been appreciated since the first years of electron crystallography that electron diffraction by crystals is mainly dominated by multiple scattering events due to the very strong interactions between the incident electron beam and the crystal nuclei and electrons (Bethe, 1928). These strong interactions provide both advantages and disadvantages for the technique of electron diffraction. It is these strong interactions that enable good statistics to be obtained from submicrometre regions (down to 2 Å). On the other hand, the strong interaction leads to the dynamical nature of electron diffraction and complicates the interpretation of electron diffraction experiments (Cowley, 1993).

In principle, if the sample used in an experiment is thin enough, the first-order kinematic theory may be applied. If its validity is assumed, the diffracted-beam amplitude for the gth diffracted beam $\mathscr{F}_g$ is then given by

$$\mathscr{F}_g \propto V_g t, \tag{1}$$

where t is the sample thickness and V_g is the gth Fourier coefficient of the crystal potential:

$$V(\mathbf{r}) = \sum_g V_g \exp(i\mathbf{g}\cdot\mathbf{r}). \tag{2}$$

In a diffraction experiment, such as an X-ray diffraction experiment, what we measure are diffracted-beam intensities rather than amplitudes. The phases associated with diffracted-beam amplitudes are lost. This is the outstanding phase problem, and a class of methods have been developed that attempt to derive the phases by mathematical means using only the intensity information (Woolfson, 1961). In many cases, however, there exist several sets of phases that fit the diffraction intensities equally well. The solution returned by using the direct methods is therefore not unique. It sometimes takes the crystallographer's chemical intuition to know which of these may be correct (Dorset, 1991).

For electron crystallographers, the situation is much more fortunate. If the diffraction experiments are performed in an electron microscope, an electron micrograph can be obtained from crystalline samples using a subset of diffracted beams. Essentially, an electron micrograph is an interference pattern formed by the selected subset of diffracted beams (Cowley, 1975; Spence, 1988). A Fourier transform of the electron micrograph then provides phases for the subset of low-resolution diffracted beams used in forming the image. With the assumption of a kinematic diffraction situation, the method of phase extension may then be used to obtain phases of higher-resolution beams observed in a diffraction pattern and to construct a higher-resolution structure map (Fan, Zhong, Zheng & Li, 1985).

For biological and organic crystals, which contain mainly weak scatterers such as C, N, O and H atoms, the use of the kinematic approximation is well justified (Unwin & Henderson, 1975; Klug, 1978/79; Dorset, 1991). Recently, however, applications of the phase-extension and Fourier method have also been made to inorganic crystals. The efficiency and correctness of the method for inorganic crystals containing strong scatterers, such as Cu and Ti atoms, have been demonstrated (Fan, Xiang, Li, Pan, Uyeda & Fujiyoshi, 1991; Zou *et al.*, 1993). This success is contradictory to the well established fact that for heavy atoms, such as Cu and Au atoms, electron diffraction by even a single atom is strongly dynamical (Glauber & Schomaker, 1953). This article aims to explain this apparent contradiction and to explore the factors that determine the validity of the direct phasing and Fourier method. In particular, we are concerned with the complex compound $C_{32}N_8Cl_{16}Cu$, which contains the heavy atoms Cu and Cl.

2. Dynamical diffraction and phase shift

To a good approximation, the scattering processess by a single atomic potential may be understood using a phase-object approximation (Cowley, 1975). Within this approximation, the electron wave function beneath an atom can be expressed as

$$\psi(\mathbf{r}) = \psi_0 q(x,y) = \psi_0 \exp[i\sigma\phi_p(x,y)], \tag{3}$$

in which ψ_0 is the incident electron wave function, $q(x,y)$ is the transmission function of the phase object, σ is the relativistic electron interaction constant, which is given by $\sigma = 2\pi me\lambda/h^2$, with all physical constants having their usual meanings, and $\phi_p(x,y)$ is the projected atomic potential in the beam direction. An analytical expression for the atomic scattering factor has been given by Doyle & Turner (1968):

$$f^e(s) = \sum_{j=1}^{4} a_j \exp(-b_j s^2), \tag{4}$$

in which $\mathbf{s} = \mathbf{g}/4\pi$, with $\mathbf{g}$ being the usual reciprocal-lattice vector, and a_j and b_j are fitting parameters. In terms of the Doyle & Turner fitting parameters, the atomic scattering potential for a high-energy electron is given by

$$\phi(x,y,z) = (h^2/2\pi m_0 e)(1/2\pi)^3 \int f^e(g/4\pi) \exp(i\mathbf{g}\cdot\mathbf{r})\, d\mathbf{g}$$

$$= (h^2/2\pi m_0 e) \sum_{j=1}^{4} a_j (4\pi/b_j)^{3/2} \times \exp[-(4\pi^2/b_j)(x^2+y^2+z^2)]. \quad (5)$$

The projected atomic potential along the z direction is given by

$$\phi_p(x,y) = \int_{-\infty}^{\infty} \phi(x,y,z)\,dz = (2h^2/m_0 e) \sum_{j=1}^{4} (a_j/b_j) \times \exp[-(4\pi^2/b_j)(x^2+y^2)]. \quad (6)$$

Using (3), we obtain the transmission function through a single atom

$$q(x,y) = \exp[i\varphi(x,y)], \quad (7)$$

with

$$\varphi(x,y) = \sigma\phi_p(x,y) = 4\pi\lambda[1+(eE/m_0c^2)] \times \sum_{j=1}^{4} (a_j/b_j)\exp[-(4\pi^2/b_j)(x^2+y^2)], \quad (8)$$

where E denotes the primary-beam energy. For a sufficiently light atom, we may take a further simplifying assumption that $\varphi \ll 1$ so that (7) may be expanded to first order to give

$$\psi(x,y) \simeq \psi_0[1+i\varphi(x,y)], \quad (9)$$

this is the weak-phase-object or kinematic diffraction approximation. The maximum phase shift φ_{max} occurs at the nucleus site, *i.e.* at $x=0$, $y=0$. An estimate of the maximum phase shift $\varphi(0,0)$ for a single atom can be made readily from (8), giving

$$\varphi_{max} = 4\pi\lambda[1+(eE/m_0c^2)] \sum_{j=1}^{4} (a_j/b_j). \quad (10)$$

Using values of Doyle & Turner (1968) for the fitting parameters a_j and b_j, we obtain for a Cu atom $\varphi_{max}(\mathrm{Cu}) = 1.35$ rad at 100 keV and $\varphi_{max}(\mathrm{Cu}) = 0.858$ rad at 500 keV. It is apparent, therefore, that the kinematic approximation is invalid even for a single atom of Cu at either 100 or 500 keV. The success of the direct phasing and Fourier method is clearly not a result of the validity of the kinematic approximation of electron diffraction in any rigorous sense.

Shown in Fig. 1 are some one-dimensional plots of the phase function $\varphi(x,y)$ along the x axis, *i.e.* $\varphi(x,0)$, for different primary-beam energies and temperatures. The calculations have been made using (8). It is seen that for all cases the kinematic approximation that leads from (7) to (9) is violated near the nucleus site at $(x,y) = (0,0)$. It should be noted, however, that the phase shift $\varphi(x,y)$ is a sharply peaked function at the nucleus site that decays exponentially from the nucleus site (see Fig. 1). At a fraction of an ångström away from the nucleus site, $\varphi(x,y)$ becomes much smaller than unity and the kinematic approximation is then well valid.

To further understand the situation as to how the kinematic approximation is broken down, it is useful to consider an analogous case of a classical collision. A collision in quantum theory is very different from a classic collision, for a quantum collision is essentially a wave phenomenon. However, if the atomic potential is sufficiently weak, a useful analogy to the scattering of a beam of classical particles by a central potential may be made (Messiah, 1972). In the classical scattering theory, an electron travels on a hyperbolic trajectory owing to the attractive Coulomb force between the electron and nucleus. The collision process is basically described by an impact parameter b, which is the nearest distance of the incident electron from the centre of the nucleus. It is a general rule that the smaller the impact distance b is, the larger the scattering angle θ will be. This fact suggests that essentially the large-angle scattering results from scattering events occurring in the area near to the nucleus. It is a corollary of this argument that the kinematic diffraction approximation is more likely to be broken down for a large-angle diffracted beam resulting from scattering events occurring near to the nucleus compared with low-angle diffracted beams resulting from scattering events occurring in a region that is distant from the nucleus. In other words, the low-index diffracted beams are more likely to result from single scattering events, while large-angle diffracted beams are likely to go through multiple scattering events.

To place the above classic argument on a more rigorous ground, we expand (7) into a power series

$$q(x,y) = 1 + i\varphi(x,y) - \tfrac{1}{2}\varphi^2(x,y) - (i/6)\varphi^3(x,y) + \ldots . \quad (11)$$

The scattering amplitude from a phase object is

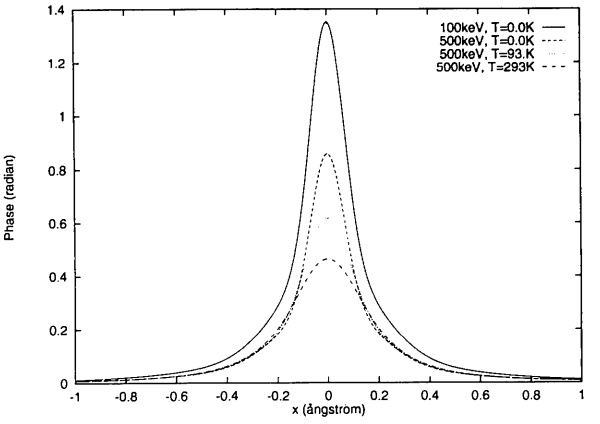

Fig. 1. Calculated phase-shift profile $\varphi(x)$ for a single Cu atom, 100 and 500 keV.

obtained by a two-dimensional Fourier transform of the transmission function minus the incident wave:

$$\begin{aligned}\mathscr{F}(k_x,k_y) &= \int[q(x,y)-1]\exp[-i(k_x x+k_y y)]\,dx\,dy \\ &= if(\mathbf{k})-\tfrac{1}{2}f(\mathbf{k})*f(\mathbf{k})-(i/6)f(\mathbf{k})*f(\mathbf{k})*f(\mathbf{k}) \\ &= \mathscr{F}_1+\mathscr{F}_2+\mathscr{F}_3+\dots\,, \end{aligned} \tag{12}$$

where the symbol * denotes the operation of convolution and $\mathscr{F}_1$, $\mathscr{F}_2$ and $\mathscr{F}_3$ represent contributions resulting from single, double and triple scattering events, respectively. In (12), $f(\mathbf{k})$ is the two-dimensional kinematic or Born scattering amplitude of a single atom:

$$\begin{aligned} f(k_x,k_y) &= \int\varphi(x,y)\exp[-i(k_x x+k_y y)]\,dx\,dy \\ &= \lambda[1+(eE/m_0c^2)] \\ &\quad\times\sum_{i=1}^{4} a_i\exp\{-[1/(4\pi)^2]b_i(k_x^2+k_y^2)\} \end{aligned} \tag{13}$$

and the single scattering amplitude is related to $f(\mathbf{k})$ *via* the relation

$$\mathscr{F}_1 = if(\mathbf{k}). \tag{14}$$

The double and triple scattering amplitudes are given by

$$\begin{aligned}\mathscr{F}_2 &= -\tfrac{1}{2}f(\mathbf{k})*f(\mathbf{k}) \\ &= -2\pi\lambda^2[1+(eE/m_0c^2)]^2\sum_{i,j=1}^{4}[a_ia_j/(b_i+b_j)] \\ &\quad\times\exp\{-[1/(4\pi)^2][b_ib_j/(b_i+b_j)](k_x^2+k_y^2)\}\end{aligned} \tag{15}$$

and

$$\begin{aligned}\mathscr{F}_3 &= -(i/6)f(\mathbf{k})*f(\mathbf{k})*f(\mathbf{k}) \\ &= -i(8\pi^2/3)\lambda^3[1+(eE/m_0c^2)^3] \\ &\quad\times\sum_{i,j,k=1}^{4}[a_ia_ja_k/(b_ib_j+b_ib_k+b_jb_k)] \\ &\quad\times\exp\{-[1/(4\pi)^2][b_ib_jb_k/(b_ib_j+b_ib_k+b_jb_k)] \\ &\quad\times(k_x^2+k_y^2)\}.\end{aligned} \tag{16}$$

Expressions (14)–(16) clearly show that, in general, the higher-order scattering amplitudes have broader angular widths compared with the lower-order amplitudes and, apart from acceleration-voltage-independent constants, the convergency of the series (11) is determined by a parameter

$$\begin{aligned}p &= \lambda[1+(eE/m_0c^2)] \\ &= h[1+(eE/m_0c^2)]\{2m_0eE[1+(eE/2m_0c^2)]\}^{-1/2},\end{aligned} \tag{17}$$

which decreases with increasing acceleration voltage E. It is then expected that for a higher accelerating voltage the convergency of the Born series (11) will be improved. This is evident from Fig. 1.

Shown in Fig. 2 are plots of single, double and triple scattering amplitudes as functions of the momentum transfer $\mathbf{q} = \mathbf{k} - \mathbf{k}_0$, in which $\mathbf{k}_0$ and $\mathbf{k}$ are the electron wave vectors for the incident and scattered electrons, respectively. Fig. 2(*a*) is calculated for 500 keV and a single Cu atom at 0 K. Shown in Fig. 2(*b*) are similar plots, but the calculations have been made for 100 keV incident electrons. Both Fig. 2(*a*) and Fig. 2(*b*) show that, while the lower-order scattering amplitudes are much larger in comparison with higher-order scattering amplitudes for small scattering angles or small q ($=\sin\theta/\lambda$, θ being the scattering angle), the situation is reversed at larger scattering angles. This is because the higher-order scattering amplitudes have broader angular widths than the lower-order scattering amplitudes. For 500 keV incident electrons, it is seen in Fig. 2(*a*) that the double scattering amplitude exceeds the single scattering amplitude at approximately 6.0 Å^{-1} and the triple scattering amplitude exceeds the single scattering amplitude at around 8.0 Å^{-1}. For a lower acceleration voltage, the situation is more severe. Fig. 2(*b*) shows that for 100 keV the double scattering amplitude exceeds the single scattering amplitude at about 4.5 Å^{-1} and the triple scattering amplitude exceeds the single scattering amplitude at 6.0 Å^{-1}. In all cases, the double scattering amplitude is seen to have comparable magnitude to the single scattering amplitude for $q > 2.0$ Å^{-1}, and the Born series is expected to break down and the kinematic approximation fails for all beams with $q > 2.0$ Å^{-1}.

Shown in Fig. 3 are variations of the phase shifts of the scattering amplitudes by a single Cu atom for 500 and 100 keV. To a rough approximation, the curves may be approximated as linear functions of the scattering angle. Detailed studies further show that the slope of the curve is approximately proportional to the atomic number (Glauber & Schomaker, 1953).

3. Phase shift and structure determination

Phase shifts have profound implications for structure determinations using electron diffraction. In general, we can write the dynamical scattering amplitude for a single atom as

$$\mathscr{f}(\mathbf{q}) = f(\mathbf{q})\exp[i\zeta(\mathbf{q})], \tag{18}$$

where $f(\mathbf{q})$ is the absolute magnitude of the scattering amplitude and $\zeta(\theta)$ is the phase shift resulting from dynamical diffraction events. For electron diffraction by an assembly of atoms, *e.g.* in the case of gas diffraction (for a review see Hargittai, 1993), the dynamical scattering amplitude is given by

$$\mathscr{f}(\mathbf{q}) = \sum_i f_i(\mathbf{q})\exp[i\zeta(\mathbf{q}) - i\mathbf{q}\cdot\mathbf{r}_i] \tag{19}$$

and the intensity distribution of scattered electrons is

$$I(\mathbf{q}) = \sum_i \sum_j f_i(\mathbf{q}) f_j(\mathbf{q}) \exp\{i[\zeta_i(\mathbf{q}) - \zeta_j(\mathbf{q})] - i\mathbf{q}\cdot(\mathbf{r}_i - \mathbf{r}_j)\}. \quad (20)$$

For gas diffraction, the molecules in the gas are randomly oriented and all orientations appear with equal probability. The intensity of the scattered electrons averaged over the random orientations of the gas molecules is given by

$$\begin{aligned} I(q) &= (1/4\pi)\int_0^{2\pi} \mathrm{d}\phi \int_0^{\pi} I(\mathbf{q}) \sin\theta \, \mathrm{d}\theta \\ &\simeq \sum_i \sum_j f_i(\mathbf{q}) f_j(\mathbf{q}) \{[\sin q(r_0 + \delta)/qr_0] \\ &\quad - [\sin q(r_0 - \delta)/qr_0]\}, \end{aligned} \quad (21)$$

where the phase shift $\zeta(q)$ has been assumed to be a linear function of the scattering angle, *i.e.*

$$\zeta_i(q) - \zeta_j(q) \simeq q\delta, \quad (22)$$

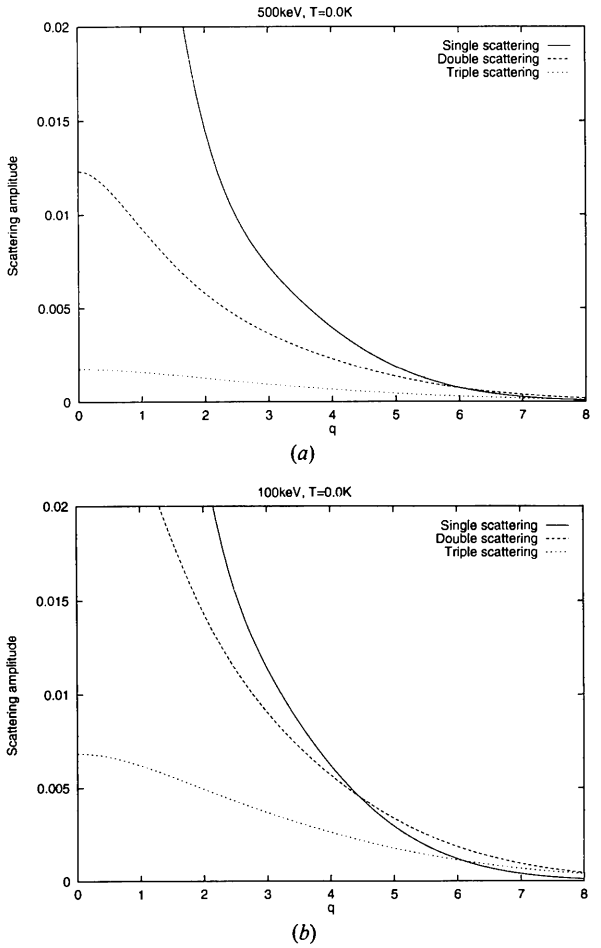

Fig. 2. Calculated momentum dependence of the single, double and triple scattering amplitudes for (*a*) 500 and (*b*) 100 keV. The unit for the scattering amplitude is Å and that for the momentum q is $Å^{-1}$.

and $r_0 = |\mathbf{r}_i - \mathbf{r}_j|$. Expression (21) is of just the form that would be given by atom pairs of split distances $r_{ij} = r_0 - \delta$ and $r_{ij} = r_0 + \delta$. If the result (21) is interpreted by the kinematic theory assuming a zero phase shift, it can lead to an erroneous conclusion that bond lengths are split, *i.e.* $r_{ij} \rightarrow r_{ij} \pm \delta$ (Glauber & Schomaker, 1953).

For crystal diffraction, the crystal structure factor is given by

$$\begin{aligned} F_g &= \sum_i f(g) \exp[i\zeta_i(g)] \exp(i\mathbf{g}\cdot\mathbf{r}) \\ &\simeq \sum_i f(g) \exp\{i\mathbf{g}\cdot[\mathbf{r}_i + \nabla_g \zeta_i(0)] + i\delta_i(0)\}, \end{aligned} \quad (23)$$

To this linear approximation of the atomic scattering amplitude phase shift, the intensity maxima in a structure map constructed from the absolute magnitude of the diffracted beams and kinematic phases will be shifted by an amount that is proportional to $\nabla_g \zeta_i$. When the linear approximation fails, the situation is more complicated and some intensity maxima that bear no direct relation to the atom positions will appear and the structure map will become an unfaithful map of the crystal structure.

4. A numerical example: chlorinated copper phthalocyanine

To illustrate how dynamical diffraction processes affect the diffracted-beam amplitudes and therefore crystal structure determinations, we now consider an example of transmission electron diffraction by a chlorinated copper phthalocyanine crystal, $C_{32}N_8Cl_{16}Cu$. The reason for our choice of this example is that previously this structure has been extensively studied in the context of electron crystallography (Uyeda, Kobayashi, Suito, Harada & Watanabe, 1972; Dorset, Tivol & Turner, 1991; Fan

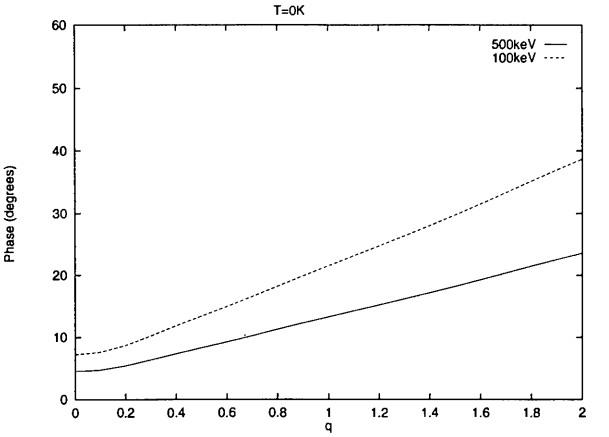

Fig. 3. Variations of the phase shift of the total scattering amplitude as a function of q for a single Cu atom and for 100 and 500 keV.

et al., 1991; Li & Tang, 1985). The unit-cell dimensions of this crystal are $a = 19.62$, $b = 26.04$, $c = 3.76$ Å and $\beta = 116.5°$. The projected structure of this crystal along the c axis is shown in Fig. 4, with the projected unit-cell parameters being $a' = a\sin\beta = 17.56$ and $b' = b = 26.04$ Å.

Shown in Figs. 5(*a*) and (*b*) are two sets of phase variations of certain diffracted-beam amplitudes. In Fig. 5(*a*), all phases of the corresponding structure factors are zero; in Fig. 5(*b*), they are 180°. The additional 90° phase shift of the diffracted beams with respect to that of the crystal structure factors is due to the factor i in (9). The calculations have been made based on the multislice formulation (Cowley & Moodie, 1957; Goodman & Moodie, 1974), using 32 768 beams and for 400 keV primary-beam energy. The first impression of these variation curves is that the phases are roughly linear functions of the crystal thickness and the slope of the linear dependence is proportional to the order of the reflection.

It should be pointed out that for small crystal thicknesses the phase variations as shown in Fig. 5 do not result from dynamical diffraction, but rather are due to a free-space propagator that has been neglected in the phase-object approximation (3). In the more sophisticated multislice approach (Cowley & Moodie, 1957), (3) is replaced by

$$\psi(x,y,z+\Delta z) = \psi_0(x,y,z)q(x,y)*P(x,y,\Delta z), \quad (24)$$

in which $P(x,y,\Delta z)$ is the Fresnel propagator (Cowley, 1975), which describes the propagation of the electron wave function from a point at (x,y,z) to an (x,y) plane at a distance Δz from the source point at (x,y,z). Under the usual high-energy small-angle approximation, the Fresnel propagator is given by

$$P(x,y,\Delta z) = (i/\Delta z\lambda)\exp[-(i\pi/\Delta z\lambda)(x^2+y^2)]. \quad (25)$$

In reciprocal space, we have

$$\mathcal{F}(k_x,k_x,z+\Delta z) = \mathcal{F}(k_x,k_y,z)P(k_x,k_y,\Delta z), \quad (26)$$

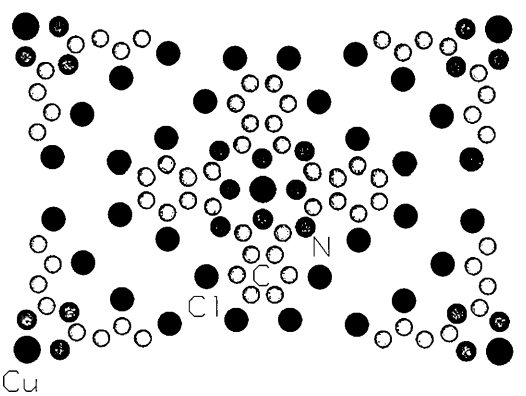

Fig. 4. Projected structure of a chlorinated copper phthalocyanine single crystal along the c axis.

in which

$$P(k_x,k_y,\Delta z) = [1/(2\pi)^2]\int P(x,y,\Delta z) \times \exp[-i(k_x x + k_y y)]\,dx\,dy = [1/(2\pi)^2]\exp[(i\Delta z\lambda/4\pi)(k_x^2+k_y^2)], \quad (27)$$

i.e. the phase variations associated with diffracted beams are proportional to Δz. For thin crystals, the scattering amplitude from a phase object is proportional to the kinematic or Born scattering amplitude which is real. Following (26), the phase shift of the diffracted beam is then proportional to the crystal thickness.

Shown in Fig. 6 are phase variation curves similar to those in Fig. 5, but the variations are corrected for the free-space propagator (27). Had the kinematic approximation been satisfied, all curves in Fig. 6 would have been horizontal straight lines. Although the curves in Fig. 6 show deviations from the perfect

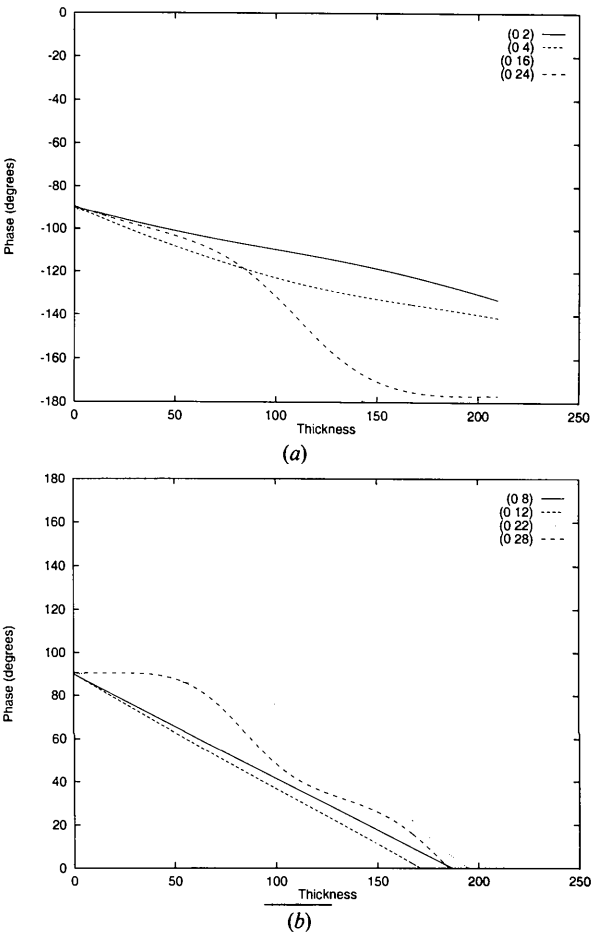

Fig. 5. Phase variations of (*a*) 0,2, 0,4, 0,16, 0,24, (*b*) 0,8, 0,12, 0,22 and 0,28 diffracted beams for 400 keV and a single $C_{32}N_8Cl_{16}Cu$ crystal.

kinematic behaviour at large thicknesses, the deviations are seen to gain appreciable magnitude only for a crystal thickness greater than 50 Å. For a crystal thicker than this, the high-index reflections 0,22 and 0,28 are seen to begin to deviate appreciably from the horizontal line and dynamical effects are expected to become important.

Shown in Fig. 7 are the corresponding variation curves of the normalized beam intensity, *i.e.* $I_g/|V_g t|^2$. Had the kinematic approximation been exactly satisfied, the normalized intensities for all beams would all have been horizontal lines. Again, it is seen that, while this perfect kinematic behaviour is not exactly reproduced, deviation from this behaviour is not very severe for a small crystal thickness.

It should be pointed out that Figs. 5, 6 and 7 have been calculated for beams of appreciable amplitudes. As a comparison, some phase and normalized beam-intensity variation curves for three weak beams have been shown in Figs. 8 and 9 as a function of crystal thickness. The relevant structure factors and those associated with Figs. 6 and 7 are given in Table 1. The kinematic behaviour is seen to be violated appreciably for a crystal thickness as small as 20 Å. This is because, while the direct kinematic routes from the incident beam to these weak beams are almost complete destructive, the alternative indirect routes that involve multiple diffraction events contribute more to the final beam amplitude. This means that multiple scattering events dominate over the single scattering processes and, consequently, the weak beams are more dynamical in nature than the low-order strong beams.

The ultimate goal of structure determinations is to find the three-dimensional atomic coordinates in real space. For high-energy electron diffraction, however, the incident electron probe is not very sensitive to the atomic coordinates along the beam direction. Electron diffraction studies thus usually aim to construct a series of faithful maps of the projected crystal structures along different orientations. A three-

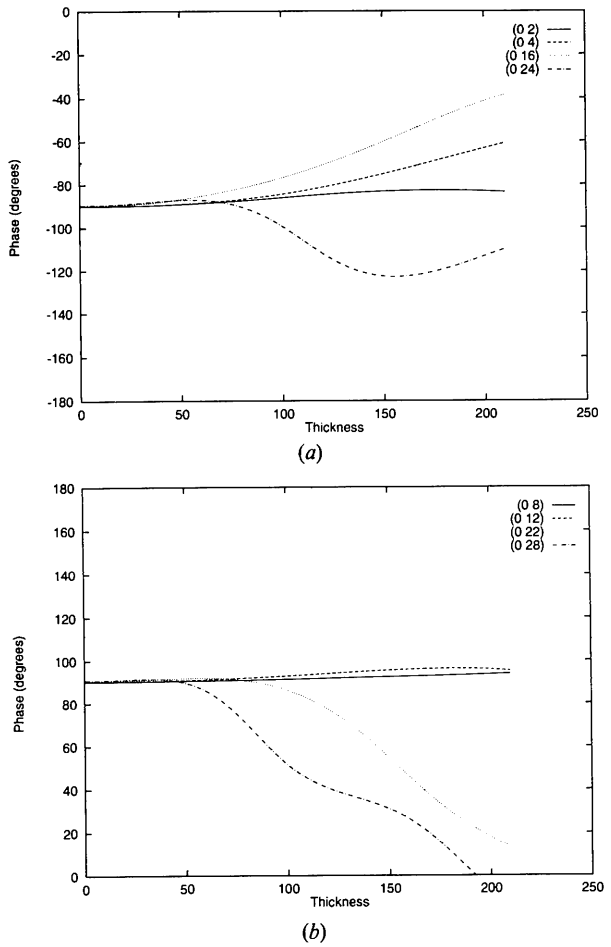

Fig. 6. Similar phase variations as Fig. 5 but the phase variation resulting from the Fresnel propagator is corrected.

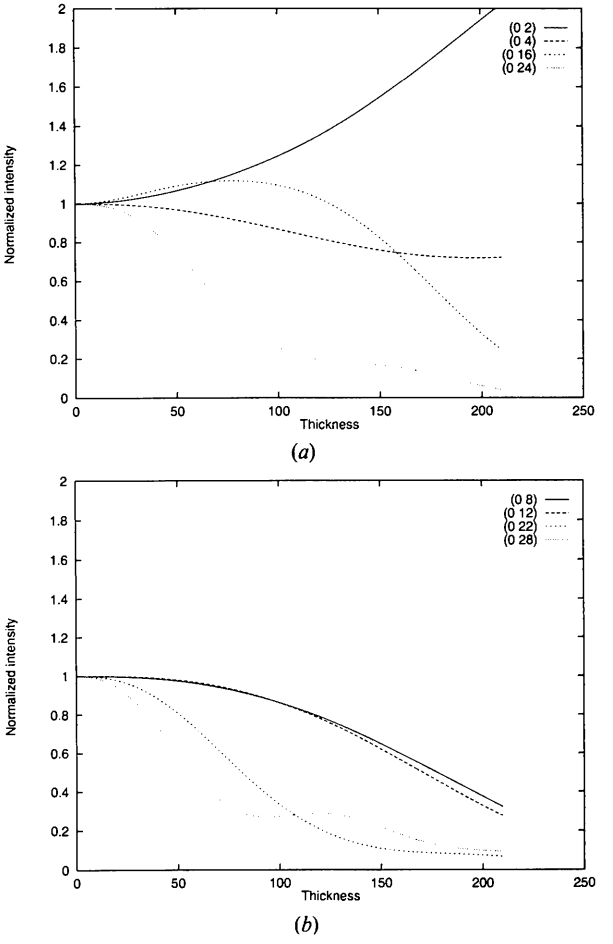

Fig. 7. Normalized beam intensities of (*a*) 0,2, 0,4, 0,16, 0,24, (*b*) 0,8, 0,12, 0,22 and 0,28 diffracted beams as against the crystal thickness. Calculations are made for 400 keV and a single $C_{32}N_8Cl_{16}Cu$ crystal.

dimensional map can then be obtained by combining these two-dimensional maps. In electron diffraction, the best possible map to construct is the electrostatic potential map, like the one shown in Fig. 10 for a $C_{32}N_8Cl_{16}Cu$ single crystal projected along the c axis.

Experimentally, if the kinematic approximation is applied, the absolute amplitude of the diffracted beam is proportional to the absolute magnitude of the relevant crystal structure factor *via* (1), *i.e.* $I_g^{1/2} = |\mathcal{F}_g| \propto |V_g|$. In a diffraction experiment, the phases associated with the diffracted beams are lost. In principle, however, these phases may be restored using direct methods (Woolfson, 1961). Assuming that the restored phases from the direct method are perfect, *i.e.* they are identical to the phases of the corresponding crystal structure factors, we can then construct a 'structure map' as follows:

$$S(x,y) = \sum_g I_g^{1/2} \exp(i\phi_g) \exp(i\mathbf{g}\cdot\mathbf{r}), \qquad (28)$$

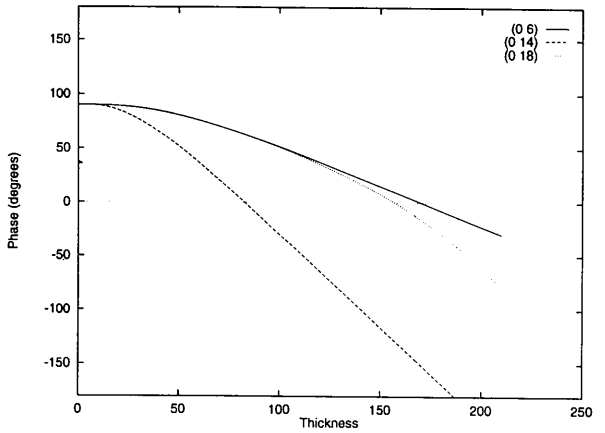

Fig. 8. Propagator-corrected phase variations for 0,6, 0,14 and 0,18 diffracted beams and 400 keV.

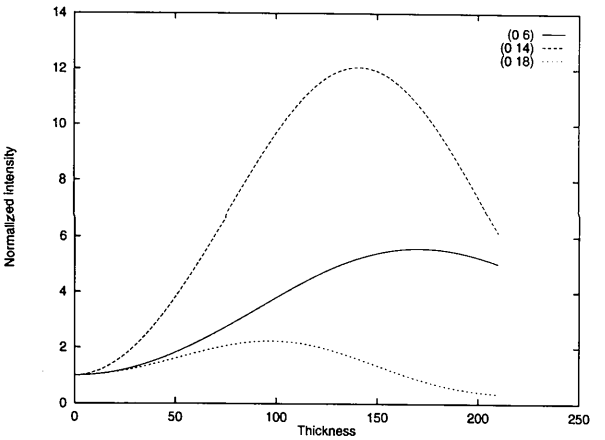

Fig. 9. Normalized beam-intensity variations corresponding to the three phase-variation curves shown in Fig. 8.

Table 1. *Structure factors*

Reflection	Amplitude (Å^{-2})	Phase (°)
020	0.010792	0.000
040	0.011677	0.000
060	0.001713	180.0
080	0.013649	180.0
0,12,0	0.017279	180.0
0,14,0	0.001510	180.0
0,16,0	0.008864	0.000
0,18,0	0.001460	180.0
0,22,0	0.009597	180.0
0,24,0	0.033634	0.000
0,28,0	0.005763	180.0

in which ϕ_g is the restored phase of the gth reflection. Given the validity of the kinematic approximation, this map is proportional to the projected potential map as shown in Fig. 10, and the two-dimensional atomic coordinates are revealed as intensity maxima in the map *via* the Poisson relation (Spence, 1993).

Alternatively, if the dynamical phases of the diffracted beams are available, as in the case of electron holography (Tonomura, 1987; Lichte, 1991), an 'electron-density map' can be constructed:

$$D(x,y) = \left|\sum_g \mathcal{F}_g \exp(i\mathbf{g}\cdot\mathbf{r})\right|^2, \qquad (29)$$

in which $\mathcal{F}_g$ is the complex amplitude of the gth diffracted beam. For both the structure and electron-density maps, the summation over g is carried out over a limited number of beams. The 'resolution' of a map is defined as the inverse of the maximum q value involved. For example, if a map is constructed using reflections with a maximum q value of 2.0 Å^{-1}, the resolution for such a map is then 0.5 Å.

Shown in Figs. 11(*a*) and (*c*) are calculated [001] electron-density maps and in Figs. 11(*b*) and (*d*) the corresponding structure maps for a single crystal of $C_{32}N_8Cl_{16}Cu$ and 400 keV primary-beam energy. Reflections with a maximum q value of 1.0 Å^{-1} are

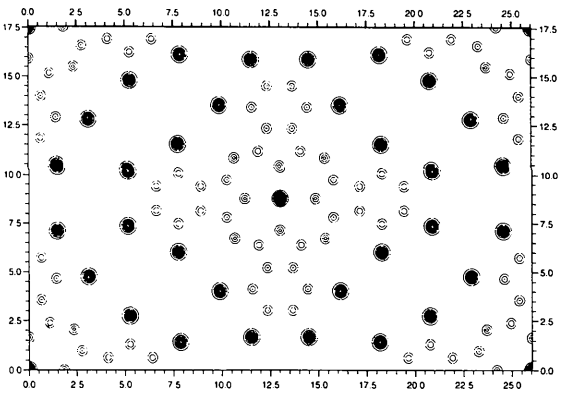

Fig. 10. Projected potential map of a cholorinated copper phthalocyanine single crystal along the c axis.

used in constructing these maps. Figs. 11(*a*) and (*b*) are calculated for a crystal thickness $t = 107$ Å, and Figs. 11(*c*) and (*d*) are calculated for a crystal thickness $t = 301$ Å. Shown in Fig. 12 are similar maps but with map resolution 0.5 Å. A general conclusion that may be drawn from these maps is that the electron-density map seems to be a more faithful representation of the crystal structure than the corresponding structure map for large crystal thicknesses.

It should be pointed out that in general the close resemblance of the electron-density map to the projected potential map cannot be taken as an indication that the kinematic approximation is valid, as can be seen from the apparent failure of the corresponding structure map to resemble the crystal potential map (see Fig. 11*d* or Fig. 12*d*). The deviation of the structure map from that of the projected potential is purely due to multiple scattering effects on the absolute magnitude of the diffracted beams (since we have assigned the kinematic phases to the diffracted beams). The reason for the tendency for the electron-density map resulting from a thick crystal to bear a resemblance to the projected potential is that in general the electron wave function in the crystal is dominated by a small number of Bloch waves, in particular the tightly bound Bloch waves (Kambe, 1982). For perfect crystals, the electron-density map is composed of contributions from these Bloch waves, with the free Bloch waves contributing only to a slowly varying background and the tightly bound Bloch waves that are localized around the atom sites contributing to the density-map contrast.

To further demonstrate the point, we show in Fig. 13 a series of four electron-density maps, calculated at crystal thicknesses of 21.5, 109.0, 215.0 and 430.0 Å, respectively, in Figs. 13(*a*), (*b*), (*c*) and (*d*). Reflections of up to 0.2 Å have been used for calculating these maps. It is seen that, for a crystal as thick as 215 Å, the correct structure can still be clearly identified from the electron-density map (Fig. 13*c*). For an even thicker crystal of 430 Å (Fig. 13*d*), the map is seen to be blurred compared with the maps constructed for a thinner crystal. Nevertheless, the map as shown in Fig. 13(*c*) still provides a fair clue to the correct atomic configuration. The deterioration of the density map with increasing crystal thickness is due to the fact that the tightly

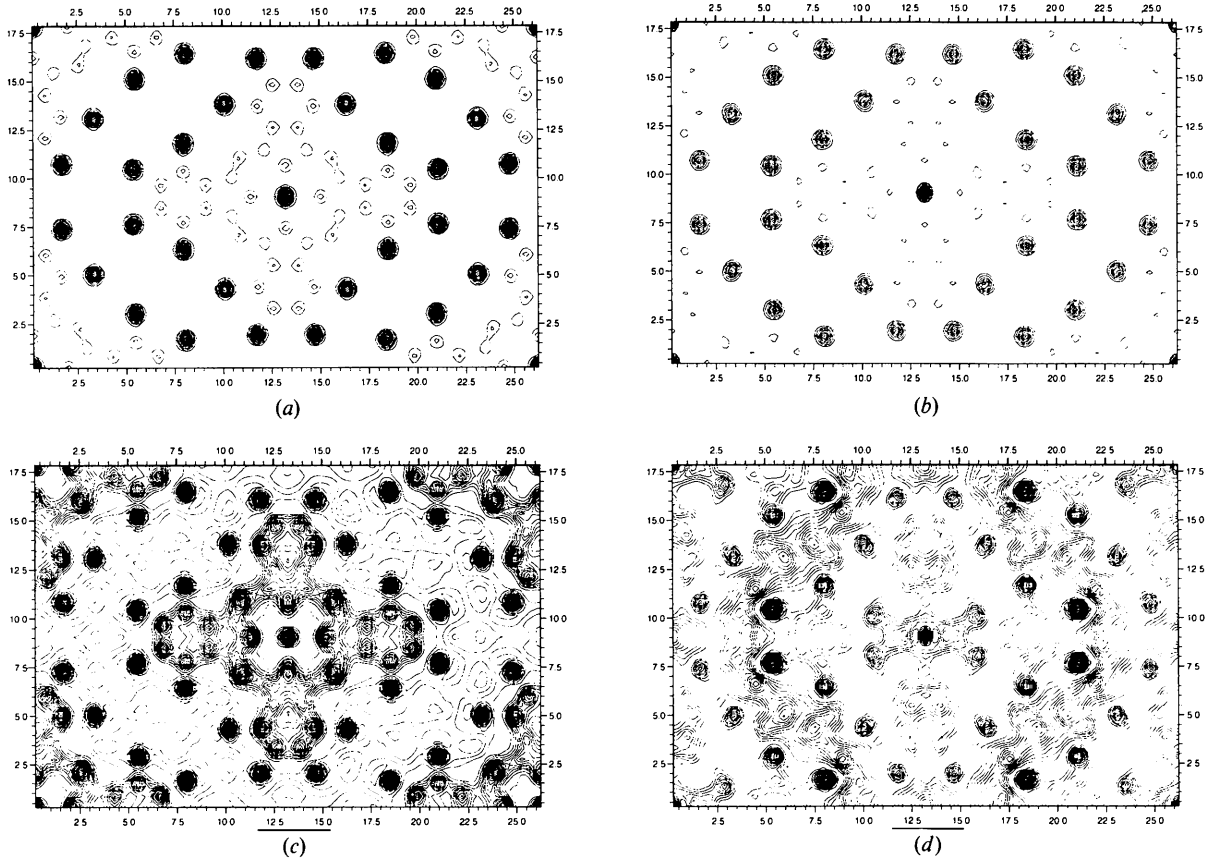

Fig. 11. Calculated electron-density maps [(*a*),(*c*)] and structure maps [(*b*),(*d*)] for 400 keV primary-beam energy, a crystal thickness of $t = 107$ Å for (*a*),(*b*) and $t = 301$ Å for (*c*),(*d*). Reflections with q up to 1.0 Å^{-1} are used for constructing the maps.

bound Bloch waves are more strongly absorbed than the free Bloch waves. As a consequence, contributions from free Bloch waves become more and more important for increasing crystal thickness. These free Bloch waves carry more information about the electron distribution in between nuclei, rather than the nuclei positions, and deteriorates the electron-density map.

As previously mentioned, for a large crystal thickness, dynamical diffraction processes will introduce phase shifts to the diffracted beams and the intensity maxima in the structure maps may not coincide with atom positions. This situation is clearly demonstrated in Figs. 11(*d*) and 12(*d*) for the 1.0 and 0.5 Å structure maps. In both maps, it is seen that many of the intensity peak positions have shifted away from the true atom positions and some additional intensity maxima that bear no relation to the crystal structure have appeared. These types of structure maps do not therefore provide faithful representation of the projected crystal potential and should not be used for direct crystal structure determination.

For a small crystal thickness, such as the one used for calculating Figs. 11(*b*) and 12(*b*), many of the low-order diffracted beams are expected to behave kinematically. A low-resolution map that uses only low-order reflections is then expected to bear close resemblance to the projected potential, except that the map is blurred compared with the projected potential map. One example is provided by the 1.0 Å-resolution structure map as shown in Fig. 11(*b*), which is seen to resemble the crystal structure fairly well. On the other hand, a higher-resolution map, such as the 0.5 Å-resolution structure map shown in Fig. 12(*b*), tends to have some intensity maxima that bear no direct relation to the maxima in the corresponding potential map. This is because the higher-order diffracted beams are affected more severely by the dynamical diffraction effects.

Previously, computer-simulated electron-microscope images of chlorinated copper phthalocyanine crystals were compared with weak-phase-object images intuitively by O'Keefe, Fryer & Smith (1983). It was found that there exists a considerable range of focus and thickness where intuitive image interpretation is possible. This conclusion is consistent with our results as presented in Fig. 13. Similar results have also been obtained by Ishizuka & Uyeda (1977), who found that a linear relationship between

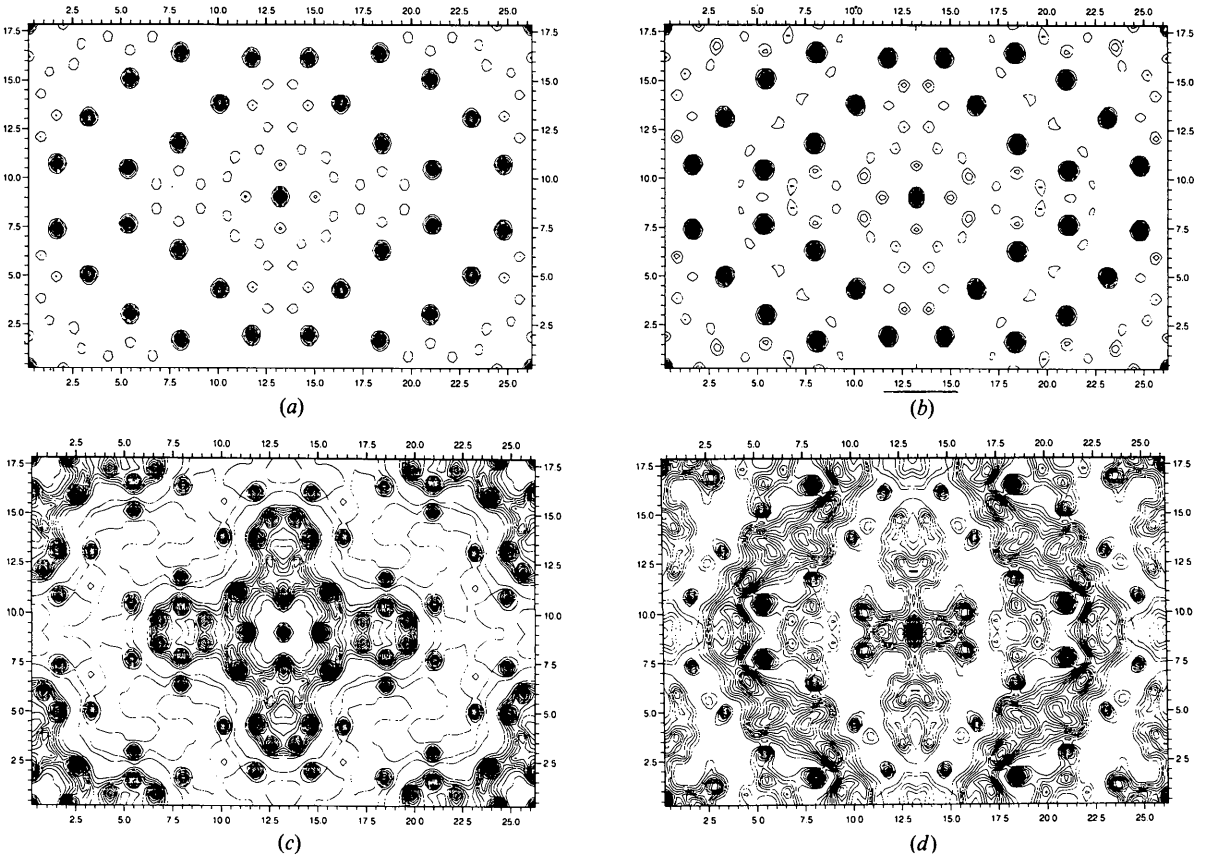

Fig. 12. Like Fig. 11 but reflections with q up to 2.0 $Å^{-1}$ are used.

the probability distribution of electrons and the specimen structure holds for a crystal having a thickness of less than 150 Å and for 100 keV, whereas the kinematic approximation breaks down for a much smaller crystal thickness. They suggested that this phenomenon should be compared to the action of a convex lens positioned at each atom location, and this is just a different way of describing the phenomenon of electron wave channelling along atom strings (see also Amelinckx & Van Dyck, 1993). The use of a dynamical Patterson function has also been discussed by Cowley & Moodie (1959), who concluded that the range of crystal thicknesses for which single-crystal structure analysis is feasible is not limited to the range of validity of the kinematic approximation. Again, this results from channelling effects.

5. Discussion

For an ordinary transmission electron microscope, the point-to-point resolution is typically about 2 Å. As discussed in the previous sections, many reflections with this order of resolution may be described using the kinematic approximation. A high-resolution electron microscopy (HREM) image obtained using relatively small angle diffracted beams will therefore provide fairly accurate kinematic phases and amplitudes for these beams. On the other hand, a diffraction pattern (which is not very sensitive to the objective-lens abberations) contains higher-resolution information when compared with a HREM image. The advantage of combining image and diffraction technique lies in the possibility that direct phase extension may be made to the higher-index diffracted beams observed in a diffraction pattern starting from the kinematic phases of low-index beams provided by a HREM image. For the higher-order beams, which are affected by dynamical diffraction, a second important fact that contributes to the success of the direct phasing and Fourier method begin to play its role. This fact is well established in the X-ray crystallography community and has been recently re-stated by Dorset (1991) in the context of electron crystallography, *i.e.* for the determination of phases using direct methods, maintaining groups of I_g in respective domains of large and weak values is much more important than is the

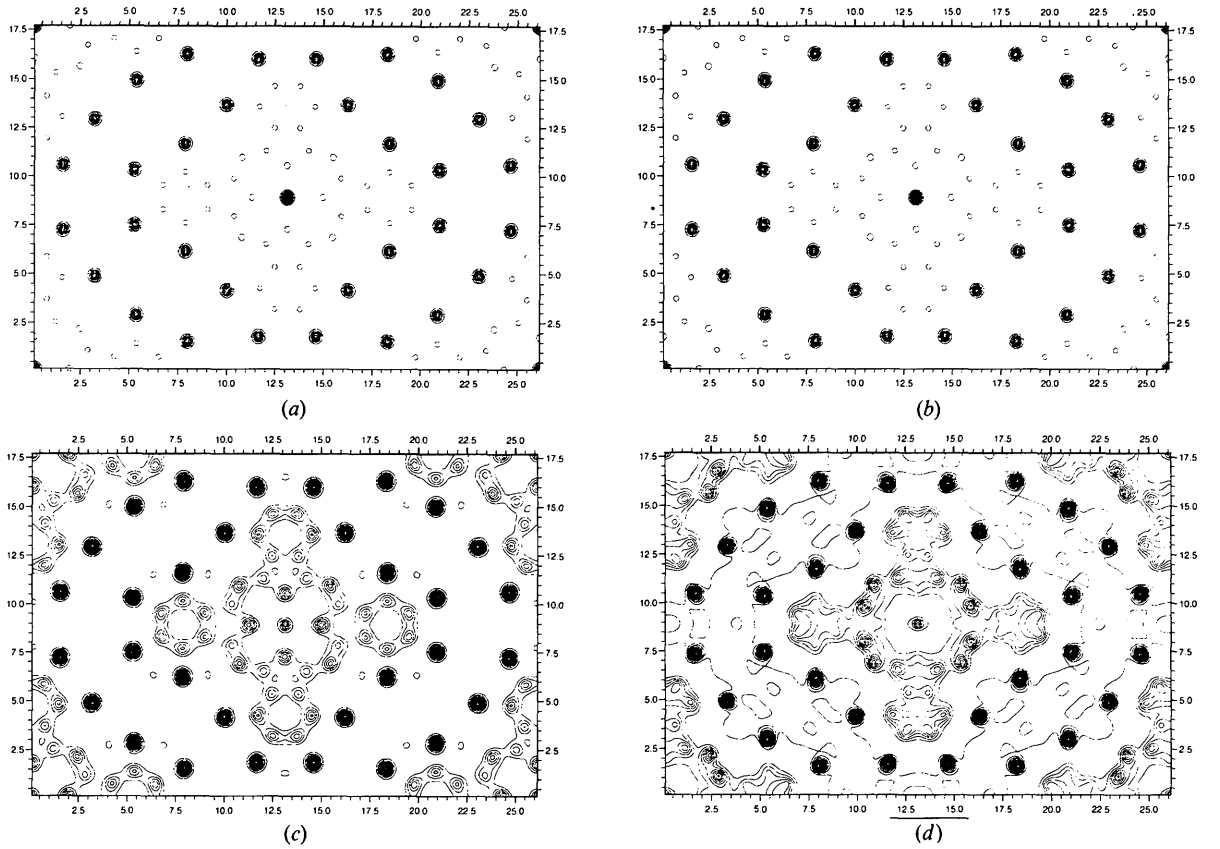

Fig. 13. Calculated electron-density maps for a crystal thickness of (*a*) 21.5, (*b*) 109.0, (*c*) 215.0 and (*d*) 430.0 Å. Reflections with q up to 5.0 $Å^{-1}$ are used.

strict hierarchical ordering of the beam intensity. The implication here is that, although the kinematic approximation is not a very accurate approximation for high-order reflections, so long as multiple scattering events do not affect the grouping of strong and weak beams, correct phases for the high-resolution reflections may still be obtained using the method of phase extension. Given correct phases and amplitudes of low-order reflections, more or less correct phases of higher-order reflections but dynamically modified absolute beam amplitudes, a last but not least fact begins to contribute to the success of the method of Fourier synthesis, *i.e.* a correct structure map depends on the phase much more sensitively than on the absolute beam amplitude. As stated most clearly by Schenk (1991): 'Even when the structure factors are all set to one or taken from another crystal the desired structure will show up in a Fourier summation, provided the correct phases have been used. However, wrong phases and correct amplitudes reveal no structure'.

6. Concluding remarks

In summary, in this paper we have shown that the kinematic approximation for electron diffraction by a compound crystal containing heavy atoms is not rigorously valid. We have shown, however, that in reciprocal space and for a thin crystal many of the low-order diffracted beams behave kinematically. Low-resolution structure maps based on these low-order diffracted beams are shown to provide a fairly faithful representation of the projected crystal potential map. On the other hand, structure maps constructed using higher-order reflections are shown to be affected more severely by dynamical diffraction effects. It is concluded that a low-resolution structure map is usually a more reliable map of the crystal structure than a high-resolution map.

In cases when the dynamical phases are available, as in the case of electron holography, an electron-density map can be constructed rather than a structure map. We have shown that for a large crystal thickness the electron-density map is usually a more faithful map of the crystal structure than the structure map. The drawbacks of the electron-density maps are that they may not be able to reveal all atom positions at one crystal thickness, and many techniques commonly used for processing the kinematic structure map, such as Fourier methods and heavy-atom methods, cannot be used to improve the dynamical electron-density map.

For a moderately thick crystal where certain dynamical effects are present, the success of the method of phase extension and Fourier synthesis for the determination of crystal structure is mainly due to three facts. Firstly, for small-angle scattering, the kinematic approximation is fairly good. A Fourier transform of a HREM image then provides rather accurate values for both phases and absolute amplitudes of the selected diffracted beams used for forming the HREM image. Secondly, the procedure of phase extension does not depend sensitively on the absolute diffracted-beam intensities but rather on the right grouping of the beam intensities. More or less correct kinematic phases may then be obtained from the procedure of phase extension for many of the large-angle diffracted beams. Thirdly, a correct structure map depends much more sensitively on the phases than on the absolute amplitudes of the structure factors, *i.e.* a correct structure map that shows up the desired structure may be obtained even though some absolute amplitudes of large-angle diffracted beams are not strictly kinematic.

This work was supported by the Violett and Samuel Glasstone Benefaction and SERC grant GR/H58278 (LMP), and the Royal Society (SQW). The authors thank Professor Sir Peter B. Hirsch, Professor M. J. Whelan and Professor K. H. Kuo for advice and encouragement, Dr X. D. Zou for drawing their attention to this problem and Professor F. H. Li, Dr R. Vincent and Dr S. Hovmöller for many stimulating discussions.

References

AMELINCKX, S. & VAN DYCK, D. (1993). *Electron Diffraction Techniques*, edited by J. M. COWLEY, Vol. II, pp. 1–218. Oxford Univ. Press.

BETHE, H. (1928). *Ann. Phys. (Leipzig)*, **87**, 55–129.

COWLEY, J. M. (1975). *Diffraction Physics*. Amsterdam: North-Holland.

COWLEY, J. M. (1993). Editor. *Electron Diffraction Techniques*. Oxford Univ. Press.

COWLEY, J. M. & MOODIE, A. F. (1957). *Acta Cryst.* **10**, 609–619.

COWLEY, J. M. & MOODIE, A. F. (1959). *Acta Cryst.* **12**, 360–367.

DORSET, D. L. (1991). *Ultramicroscopy*, **38**, 23–40.

DORSET, D. L., TIVOL, W. F. & TURNER, J. N. (1991). *Ultramicroscopy*, **38**, 41–45.

DOYLE, P. A. & TURNER, P. S. (1968). *Acta Cryst.* A**24**, 390–397.

FAN, H. F., XIANG, S. B., LI, F. H., PAN, Q., UYEDA, N. & FUJIYOSHI, Y. (1991). *Ultramicroscopy*, **36**, 361–365.

FAN, H. F., ZHONG, Z. Y., ZHENG, C. D. & LI, F. H. (1985). *Acta Cryst.* A**41**, 163–165.

GLAUBER, R. & SCHOMAKER, V. (1953). *Phys. Rev.* **89**, 667–671.

GOODMAN, P. & MOODIE, A. F. (1974). *Acta Cryst.* A**30**, 280–290.

HARGITTAI, I. (1993). In *Electron Diffraction Techniques*, edited by J. M. COWLEY. Oxford Univ. Press.

ISHIZUKA, K. & UYEDA, N. (1977). *Acta Cryst.* A**33**, 740–749.

KAMBE, K. (1982). *Ultramicroscopy*, **10**, 223–228.

KLUG, A. (1978/79). *Chem. Scr.* **14**, 245–256.

LI, F. H. & TANG, D. (1985). *Acta Cryst.* A**41**, 376–382.

LICHTE, H. (1991). *Advances in Optical and Electron Microscopy*, edited by T. MULVEY & C. J. R. SHEPPARD, Vol. 12, pp. 25–91. London: Academic Press.
MESSIAH, A. (1972). *Quantum Mechanics*, Vol. I. Amsterdam: North-Holland.
O'KEEFE, M. A., FRYER, J. R. & SMITH, D. J. (1983). *Acta Cryst.* A**39**, 838–847.
SCHENK, H. (1991). *Direct Methods of Solving Crystal Structures*, edited by H. SCHENK, pp. 1–8. New York: Plenum Press.
SPENCE, J. C. H. (1988). *Experimental High-Resolution Electron Microscopy*. Oxford Univ. Press.
SPENCE, J. C. H. (1993). *Acta Cryst.* A**49**, 231–260.
TONOMURA, A. (1987). *Rev. Mod. Phys.* **59**, 639–669.
UNWIN, P. N. T. & HENDERSON, R. (1975). *J. Mol. Biol.* **94**, 425–440.
UYEDA, N., KOBAYASHI, T., SUITO, E., HARADA, Y. & WATANABE, M. (1972). *J. Appl. Phys.* **43**, 5181–5189.
WOOLFSON, M. M. (1961). *Direct Methods in Crystallography*. Oxford: Clarendon Press.
ZOU, X. D., HOVMÖLLER, S., PARRAS, M., GONZÁLET-CALBET, J. M., VALLET-REGI, M. & GRENIER, J. C. (1993). *Acta Cryst.* A**49**, 27–35.

Acta Cryst. (1994). A**50**, 771–778

The Probabilistic Estimation of Triplet Invariants: the Formula P_{13}

BY M. C. BURLA

Dipartimento di Scienze della Terra, Università, 06100 *Perugia, Italy*

C. GIACOVAZZO AND A. G. G. MOLITERNI

Istituto di Ricerca per lo Sviluppo di Metodologie Cristallografiche CNR, c/o Dipartimento Geomineralogico, Campus Universitario, 70124 *Bari, Italy*

AND J. GONZALEZ PLATAS

Dipartimento de Fisica Fundamental y Experimental, Universidad de La Laguna, La Laguna, Tenerife, Spain

(*Received* 15 *February* 1994; *accepted* 3 *May* 1994)

Abstract

The second representation of a triplet invariant [Giacovazzo (1977). *Acta Cryst.* A**33**, 933–944] is a collection of special quintets. In the present paper, the triplet is embedded in many more additional quintets obtained in a special way by symmetry operations on the indices of the structure factors. The method of joint probability distribution functions has been used to derive a formula for estimating triplets *via* the information contained in the basis and in the cross terms of the quintet invariants. The P_{10} formula [Cascarano, Giacovazzo, Camalli, Spagna, Burla, Nunzi & Polidori (1984). *Acta Cryst.* A**40**, 278–283] is a special case of the new formula, here called P_{13}. The new expression has been applied to practical cases.

Symbols and abbreviations

$\mathbf{C} \equiv (\mathbf{R},\mathbf{T})$	Symmetry operator. $\mathbf{R}$ is the rotation component, $\mathbf{T}$ is the translation component.
$E_{\mathbf{h}} = \lvert R_{\mathbf{h}}\rvert \exp(i\varphi_{\mathbf{h}})$	Normalized structure factor.
$\varepsilon_{\mathbf{h}} = R_{\mathbf{h}}^2 - 1$	
$\Phi_3 = \varphi_{\mathbf{h}_1} + \varphi_{\mathbf{h}_2} + \varphi_{\mathbf{h}_3}$	With $\mathbf{h}_1 + \mathbf{h}_2 + \mathbf{h}_3 = \mathbf{0}$.
m	Number of symmetry operators.
N	Number of atoms in the primitive unit cell.
$D_1(x) = I_1(x)/I_0(x)$	Ratio of the two modified Bessel functions of order 1 and 0, respectively.

Introduction

In accordance with Giacovazzo (1977), the second representation $\{\psi\}_2$ of the triplet phase invariant Φ_3 is the collection of special quintets

$$\psi_2 = \Phi_3 + \varphi_{\mathbf{kR}_i} - \varphi_{\mathbf{kR}_i}, \quad i = 1,....,m, \qquad (1)$$

where $\mathbf{k}$ is a free vector in reciprocal space. The collection of the basis and cross magnitudes of the various quintets ψ_2 is called the second phasing shell of Φ_3:

$$\{B\}_2 = \{R_{\mathbf{h}_1}, R_{\mathbf{h}_2}, R_{\mathbf{h}_3}, R_{\mathbf{k}}, R_{\mathbf{h}_1 \pm \mathbf{kR}_i}, R_{\mathbf{h}_2 \pm \mathbf{kR}_i}, R_{\mathbf{h}_3 \pm \mathbf{kR}_i}\}, \quad i = 1,...,m.$$

A formula was derived (Cascarano, Giacovazzo, Camalli, Spagna, Burla, Nunzi & Polidori, 1984) that can be used to estimate Φ_3 given the moduli in $\{B\}_2$:

$$P(\Phi_3|\{B\}_2) \simeq [2\pi I_0(G)]^{-1} \exp(G \cos \Phi_3),$$